JOURNAL OF AIRCRAFT
Vol. 32, No. 6, November–December 1995

Unsteady Characteristics of a Hypersonic Type IV Shock Interaction

Charles A. Lind* and Mark J. Lewis†
University of Maryland, College Park, Maryland 20742

The unsteady characteristics of a Mach 8 type IV shock interaction are numerically studied using a time-accurate total variation diminishing scheme for solving the thin layer approximation to the two-dimensional Navier–Stokes equations in conservative form. The calculations show that the peak surface pressure, the impingement location of the supersonic jet, and the time required for the development of the interaction are strong functions of the impinging shock location. For a range of impinging shock locations the interaction is found to be unsteady. In addition, this unsteady phenomena is shown to be related to the transients of the interaction and to the orientation of the terminating shock associated with the supersonic jet. The frequency of oscillation of the supersonic jet, as described by the location of the peak surface pressure, is shown to be proportional to the location of the impinging shock.

Nomenclature

A, B	=	grid clustering parameters
D, H	=	grid clustering parameters
M	=	Mach number
p	=	pressure
Re	=	Reynolds number
T	=	temperature
t	=	time
x, y	=	physical coordinates
β	=	shock angle
$\Delta( )$	=	change in ( )
θ	=	angular measurement
ρ	=	density

Subscripts

j	=	jet
s	=	shock
w	=	wall
0	=	stagnation
∞	=	freestream

Introduction

THE successful design of a hypersonic vehicle will depend on the accurate prediction of the interaction between the oblique shocks formed on its primary surfaces and the curved shocks formed on its protruding surfaces. This configuration is like that of the proposed hypersonic, transatmospheric vehicle, shown in Fig. 1, or of the hypersonic waverider.[1]

Since these vehicles will require aerodynamic control surfaces, as well as an engine-integrated airframe to successfully complete their missions, an environment will exist for the formation of detached, curved shocks. The interaction of the vehicles straight oblique shocks with its curved shocks can result in a very complex flowfield with extremely high pressure and heat transfer rates within an extremely localized region (i.e., a type IV shock interaction). Experimental as well as computational results have shown that these pressure loads and intense heating rates can be up to 30 times larger than those of the noninterfering case.[2–8] The associated large-temperature gradients and attendant thermal stresses resulting from this interaction may severely limit the useful life of the structural components, which in turn could limit the usefulness of the vehicle.

The type IV shock interaction is one of the six types of shock interactions first categorized by Edney in 1968.[2] The six different shock interaction patterns are shown in Fig. 2 and the type IV shock interaction is described in more detail in Fig. 3. It has been experimentally shown that for the type IV shock interaction, the peak pressure, heat transfer rate, and surface pressure distributions are sensitive to upstream thermodynamic flow conditions, shock strength, and Mach number.[2,3,8–10] In addition, recent experimental[3,11] and computational[5–8,12] work suggests that the type IV interaction is unsteady. Verifying the unsteadiness and identifying the characteristics of the unsteady phenomena is important from a structural standpoint. The cooling requirements will strongly depend on whether or not the supersonic jet is fixed or oscillating, and, more importantly, structural fatigue may set in if the leading edges are not properly designed for the periodic heating of the structure due to the oscillating supersonic jet.

This work considers the effect the location of the impinging shock has on the type IV shock interaction, in particular, the unsteady phenomena associated with the interaction. The var-

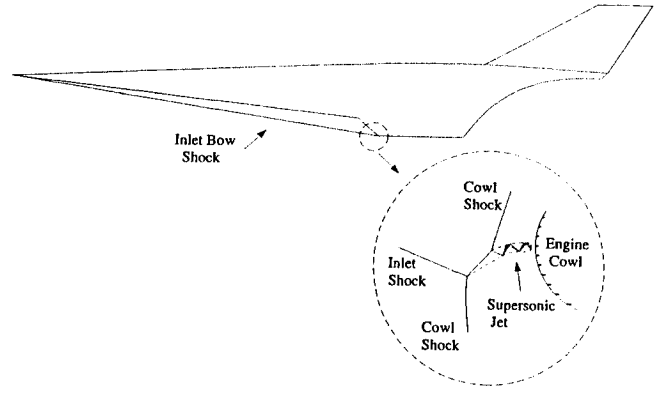

Fig. 1 Generic hypersonic vehicle showing the type IV shock interaction.

Presented as Paper 94-2945 at the AIAA/ASME/SAE/ASEE 30th Joint Propulsion Conference and Exhibit, Indianapolis, IN, June 27–29, 1994; received Aug. 10, 1994; revision received April 11, 1995; accepted for publication May 15, 1995.

*Graduate Research Assistant; currently ONR Postdoctoral Fellow, Department of Aerospace Engineering, U.S. Naval Academy, Annapolis, MD 21402-5042. Member AIAA.

†Assistant Professor, Department of Aerospace Engineering. Member AIAA.

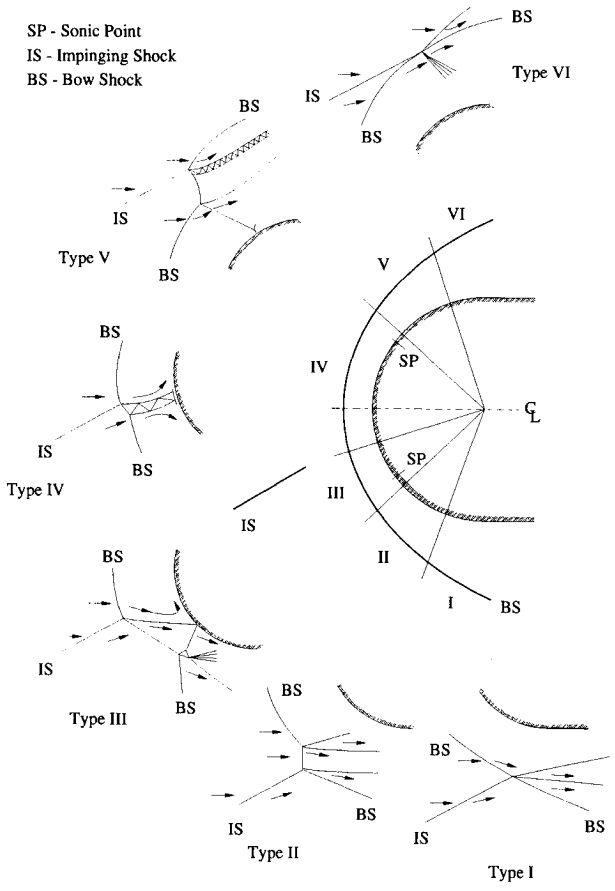

Fig. 2 Six types of shock interaction patterns.

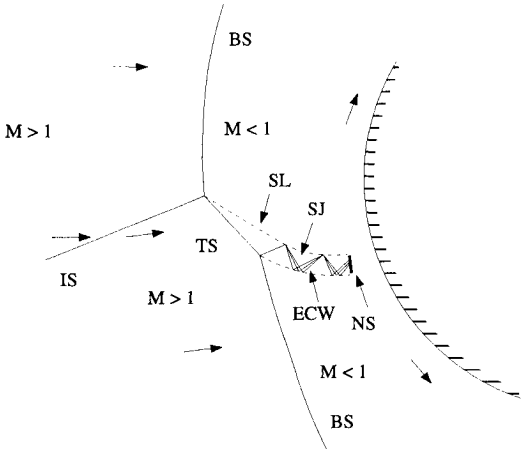

BS - Bow Shock
ECW - Expansion / Compression Waves
IS - Impinging Shock
NS - Normal Shock
SL - Shear Layer
SJ - Supersonic Jet
TS - Transmitted Shock

Fig. 3 Type IV shock interaction.

iation of the peak surface pressure with time is considered, as is the time evolution of the interaction. Finally, a detailed flowfield analysis of the jet impingement region is performed from which conclusions can be drawn about possible causes of the unsteadiness associated with the interaction.

Numerical Algorithm

The approach to high resolution upwind schemes is incorporated in the prevention of numerical oscillations, as opposed to classical methods where oscillations are damped out after they have occurred. For this reason, a high resolution scheme, in particular the total variation diminishing (TVD) algorithm, was selected for this work and is described in detail by Lind.[8]

The original TIMETVD code, which forms the basis for the present work, was derived from the ARC2D code developed by Steger and Pulliam[16] at the NASA Ames Research Center. The ARC2D code solves the thin layer approximation to the Navier–Stokes equations in generalized curvilinear coordinates. Helen Yee,[14] also of NASA Ames, modified the inviscid portion of ARC2D with the TVD algorithm. The numerical algorithm is an implicit approximate factorization finite difference scheme (ADI). The TVD scheme used in the present work, which was developed by Yee and Harten[13] and Yee,[14] gives second-order accuracy in space and time. Roe's[15] averaging is used to describe the inviscid components of the flux. The entropy fix of Harten, with Yee's second-order corrections is implemented and the explicit viscous terms are centrally differenced.

The original ARC2D code has been validated by Pulliam,[16] the original TIMETVD code by Montagne and Yee,[17] and the present version of the TIMETVD code by Lind.[8]

Initial and Boundary Conditions

In order to initiate the time-accurate solution of the shock interaction, a blunt-body solution (i.e., no impinging shock) is first calculated. A straight oblique shock (of a given strength defined by the shock angle β) is then introduced into the flowfield such that it intersects the shock formed on the blunt body at an angle given by θ_s, as shown in Fig. 4. For all calculations a zero pressure gradient and constant temperature are assumed at the body surface.

The outflow boundary, which is supersonic for all calculations, is extrapolated from the adjacent grid point. For the blunt-body calculation freestream values are used for all points on the inflow boundary. For the shock interaction cases freestream conditions are assigned to the points on the inflow boundary above the shock impingement point and values given by the Rankine–Hugoniot equation for the given freestream Mach number and shock angle are assigned to the remaining inflow points.

Grid Generation

A two-step grid generation process, an algebraic grid followed by an elliptic smoother, was used. The algebraic grid algorithm generated the body, the outside boundary, and clustered grid points circumferentially in regions of interest. Specifically, the points on the outside boundary were clustered near the impinging shock location and points on the solid boundary were clustered near the impingement point of the supersonic jet. An elliptic solver was utilized to assure

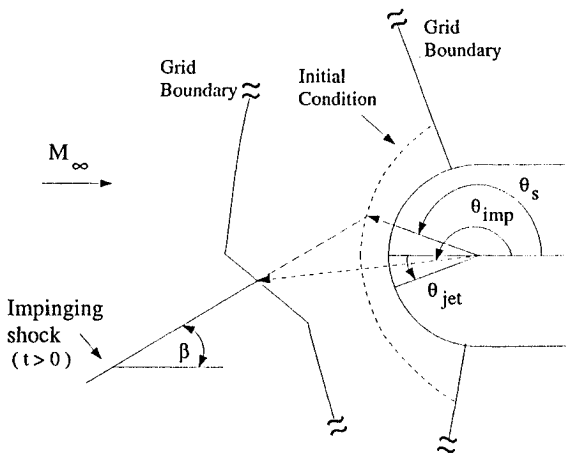

Fig. 4 Nomenclature used in the discussion.

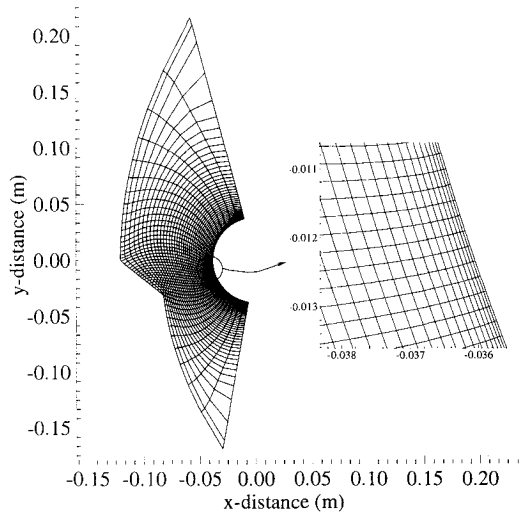

Fig. 5 Typical 181 × 160 elliptic grid. (Note: every 4th point in the ξ and η direction is shown.) Inset highlights the body region (every grid point is shown).

smoothness of the grid, orthogonality of the grid lines at the solid surface, and grid clustering at the solid boundary.

Algebraic Grid Generation

The solid body was modeled as a circular cylinder. The freestream boundary was generated using the shock correlations of Billig.[18] The upper and lower portions of the outside boundary were calculated independently, so to conform to the geometry of the type IV interaction, and were connected by a straight line.

Clustering in the circumferential direction was performed separately on the surface and freestream boundaries and was accomplished by using the following stretching function from Hoffmann[19]:

$$x = \xi$$

$$y = D\left\{1 + \frac{\sinh[B(\eta - A)]}{\sinh(BA)}\right\} \tag{1a}$$

where A is given by

$$A = \frac{1}{2B}\ln\frac{1 + (e^{B} - 1)(D/H)}{1 + (e^{-B} - 1)(D/H)} \tag{1b}$$

In Eqs. (1a) and (1b), B is the grid clustering parameter and controls the amount of clustering, H is the total length of the direction being considered, D is the y coordinate where clustering is desired, and ξ and η are the coordinates in the computational space.

Elliptic Grid Generation

In order to ensure orthogonality at the solid surface and also to smooth the grid, the elliptic grid generation algorithm developed by Sorenson[20] was used. In addition to grid orthogonality, the algorithm also allowed the user to specify the spacing between the solid body and the grid point immediately above it. A typical grid used in this study is shown in Fig. 5.

Results

Initial Blunt-Body Solutions

Recall that a blunt-body solution is used as the initial condition for the calculation of the type IV shock interaction. This calculation was considered converged when the L_2 norm of the density residual dropped below 10^{-10}. The L_2 norm of the density residual is defined as

$$\|\rho_r\|_2 = \frac{\sqrt{\sum_{j=1}^{j\max}\sum_{k=1}^{k\max}(\rho_{rj,k})^2}}{\sqrt{j_{\max}k_{\max}}\,\Delta t} \tag{2}$$

where $\rho_{rj,k}$, the residual of the density, is the difference in the value of density between two time integration steps

$$\rho_{rj,k} = \rho_{j,k}^{n+1} - \rho_{j,k}^{n} \tag{3}$$

It has been suggested by Kloper and Yee[6] and Hoffmann[21] that the calculation of heat transfer is a function of the distance from the body to the first grid point $\Delta\eta_w$, and that the pressure is not as sensitive. In addition, they showed that accurate prediction of the pressure was possible even for grid spacing several orders of magnitude greater than that required for accurate heat transfer predictions. This trend was also noticed in the present work. In particular, the laminar flow over a blunt body was calculated and compared with the experimental results of Holden,[22] run 31. In particular, $M_\infty = 8.033$, $T_\infty = 404.64$ K, $T_w = 954.0$ K, and $Re/m = 4.911 \times 10^6$. The results are shown in Figs. 6a and 6b for several values of $\Delta\eta_w$ and they clearly show this trend.

In order to accurately predict the heat transfer in this work it is estimated that $\Delta\eta_w$ would have to be at least 10^{-9} m. Since grid spacing of this order would drastically increase the computational effort and, moreover, since this work is directed more towards the understanding of the unsteady phenomena associated with the interaction (which pressure measurements can accurately analyze), heat transfer was not calculated.

Parametric Studies

A series of numerical experiments was performed in which the value of the impinging shock location θ_s was varied be-

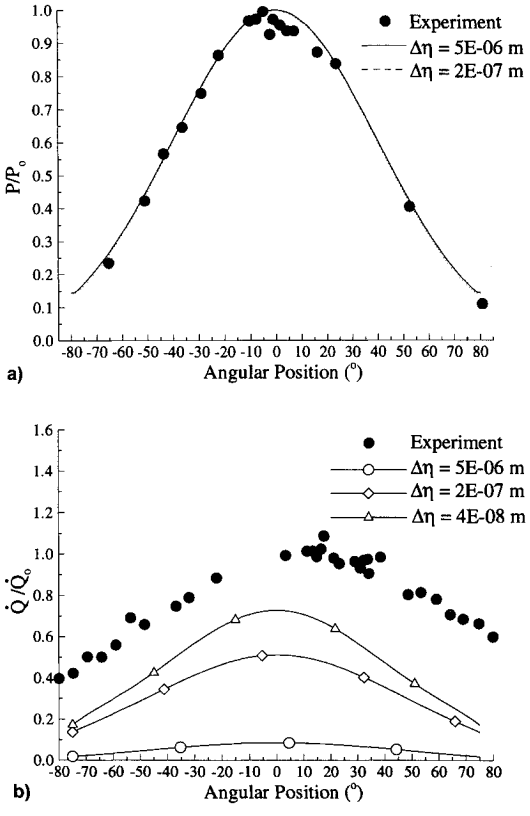

Fig. 6 Comparison of calculated a) surface pressure and b) heat transfer with experiment.

tween the values of 168–186 deg. The flow conditions are modeled after those of Holden,[22] run 24. Specifically, the following values were used: $M_\infty = 8.144$, $T_\infty = 429.12$ K, $Re/m = 1.243 \times 10^7$, $T_w = 954.0$ K, and $\Delta\eta_w = 3.4 \times 10^{-5}$. Furthermore, the calculations were performed with an impinging shock angle of 19 deg and all calculations were performed on a 181 × 160 grid. The computations presented in this work are summarized in Table 1. In this table the maximum Courant–Friedrichs–Lewy number, CFL_{max}, corresponds to the maximum CFL for the calculation. Since the value of CFL varies with time, only the maximum value is referenced in the table.

Table 1 Summary of results using 181 × 160 grid

θ_s, deg	JIA, deg	P/P_0	Δt, $\times 10^{-7}$ s	CFL, max	Notes
168.2	10.98	9.88	2.00	4.5	—
170.0	13.43	10.07	2.00	4.5	—
171.2	14.96	10.11	2.00	4.4	—
174.0	17.59	10.10	2.00	4.4	—
175.7	18.90	10.08	1.32	2.9	*U*
179.1	20.98	9.98	2.00	3.3	—
182.9	23.82	9.79	2.00	4.5	*U*
185.9	27.0	9.78	2.00	4.5	*U*

Note: JIA and P/P_0 correspond to steady-state values, $\beta = 19$ deg and $U \equiv$ unsteady.

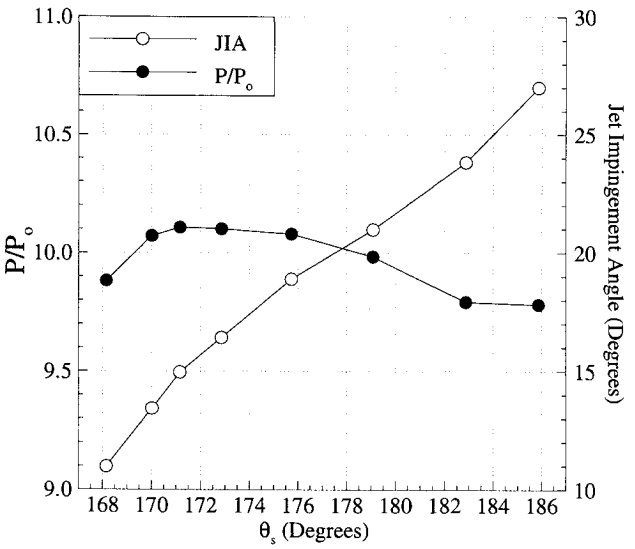

Fig. 7 Effect of θ_s on the peak pressure and jet impingement angle.

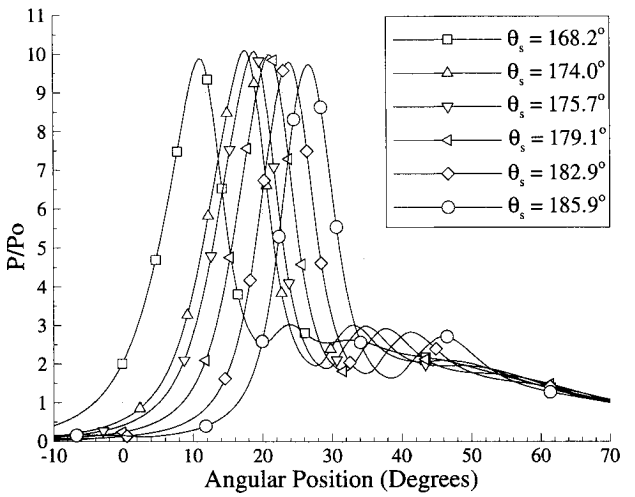

Fig. 8 Comparison of surface pressure for $168.2 \leq \theta_s \leq 185.9$ deg ($-10 \leq \theta \leq 70$ deg).

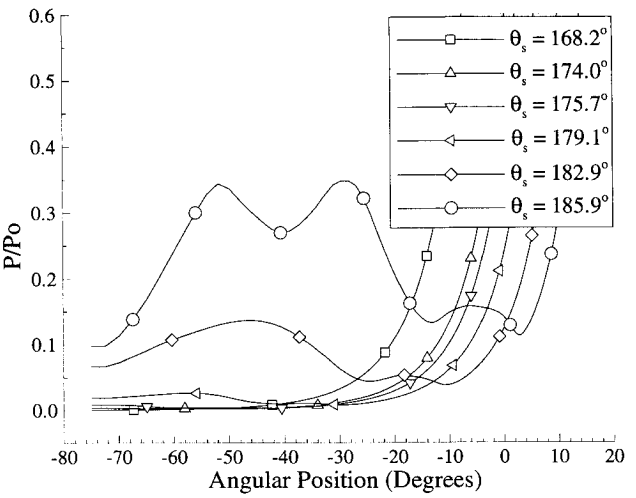

Fig. 9 Comparison of surface pressure for $168.2 \leq \theta_s \leq 185.9$ deg ($-80 \leq \theta \leq 20$ deg).

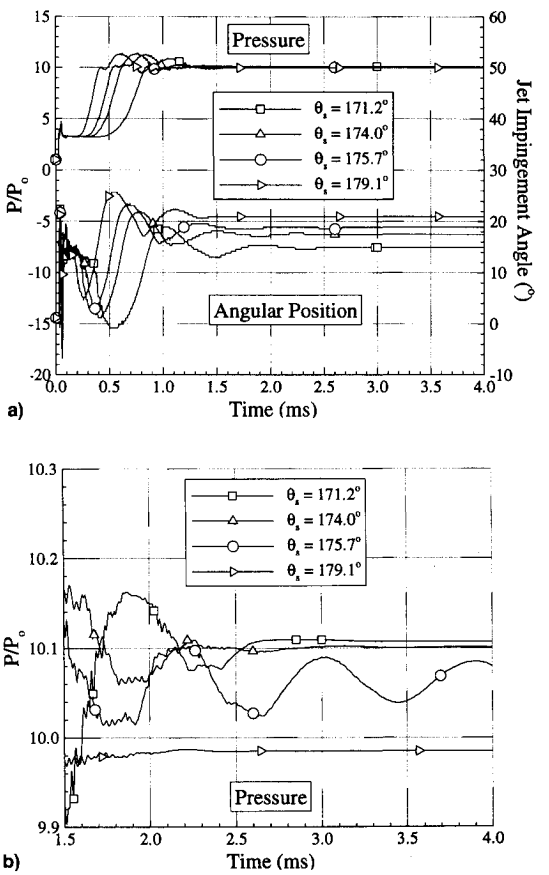

Fig. 10 Time variation of peak pressure and jet impingement location for different shock impingement locations: a) full view and b) close view of pressure.

Figure 7 shows the variation of the peak surface pressure and the angle at which the supersonic jet impinges the surface, given by the location of the peak surface pressure, for the various shock impingement angles θ_s. The trends shown are not unexpected. First, as the location of impinging shock moves downward (from $\theta_s < 180$ deg to $\theta_s > 180$ deg) the impingement location of the supersonic jet also moves downward. In addition, the peak surface pressure reaches a maximum, which is also expected since the other types of interactions have a

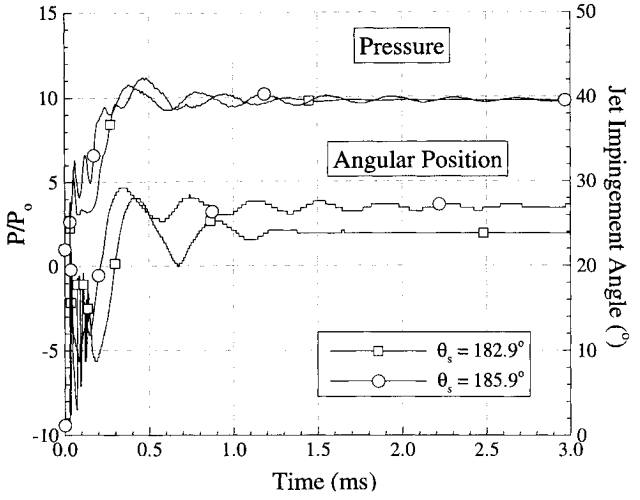

Fig. 11 Time variation of peak pressure and jet impingement location for $\theta_s > 180$ deg.

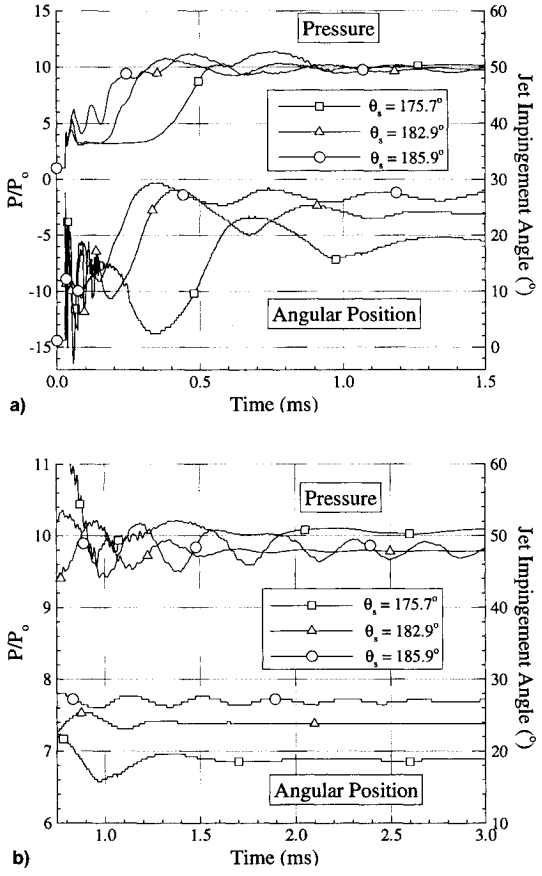

Fig. 12 Time variation of peak pressure and jet impingement location for the unsteady calculations: a) $0.0 \leq t \leq 1.5$ ms and b) $0.75 \leq t \leq 3.0$ ms.

lower peak surface pressure than that of the type IV interaction.

Figures 8 and 9 show the surface pressure distribution for different shock impinging locations in the range $168.2 \leq \theta_s \leq 185.9$ deg. Figure 8 highlights the distribution of the peak surface pressure and Fig. 9 shows the development of an unsteady separation bubble as θ_s increases from 168.2 to 185.9 deg. The unsteady flowfield associated with $\theta_s = 185.9$ deg will be discussed in more detail later. These plots also reinforce the results shown in Fig. 7.

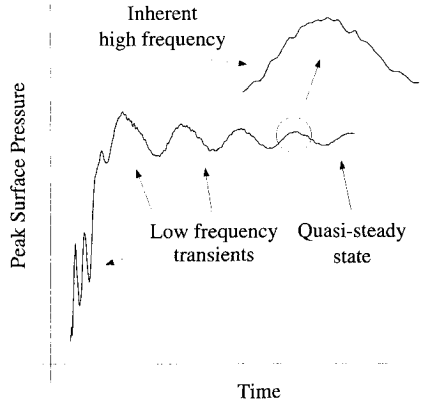

Fig. 13 Schematic of the pressure distribution with time showing types of oscillations.

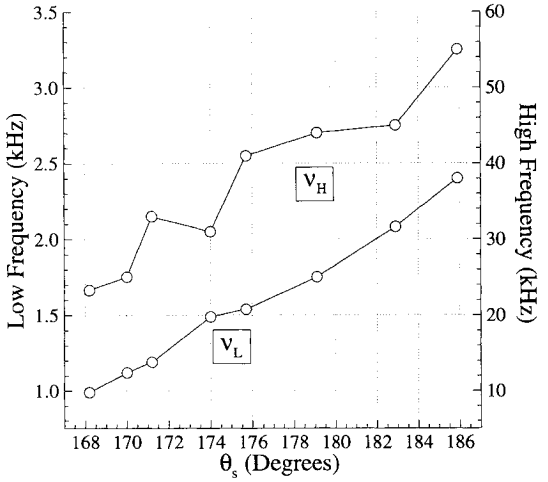

Fig. 14 Effect of θ_s on the low frequency ν_L and high frequency ν_H oscillations.

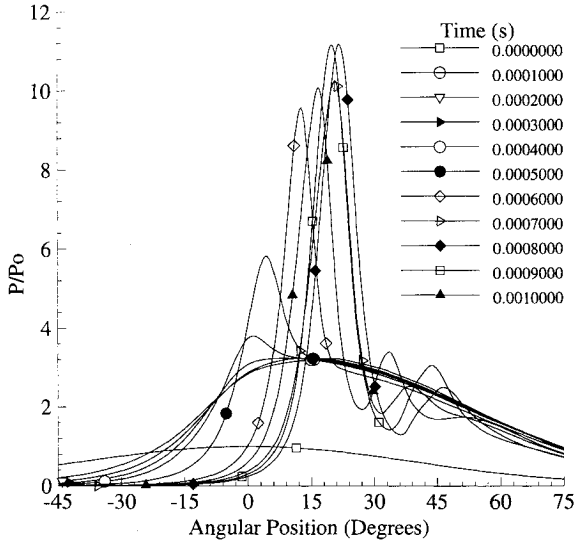

Fig. 15 Time history ($t \leq 1.0$ ms) of the surface pressure for θ_s = 174.0 deg.

Jet Unsteadiness

A time history of the peak surface pressure and its location are considered for several shock impingement positions ($168.2 \leq \theta_s \leq 185.9$ deg) and are shown in Figs. 10–12. The results for some of the cases where $\theta_s < 180$ deg are shown in Fig. 10. Notice that some cases resulted in flowfields in which the transients of the interaction subsided, as given by the value

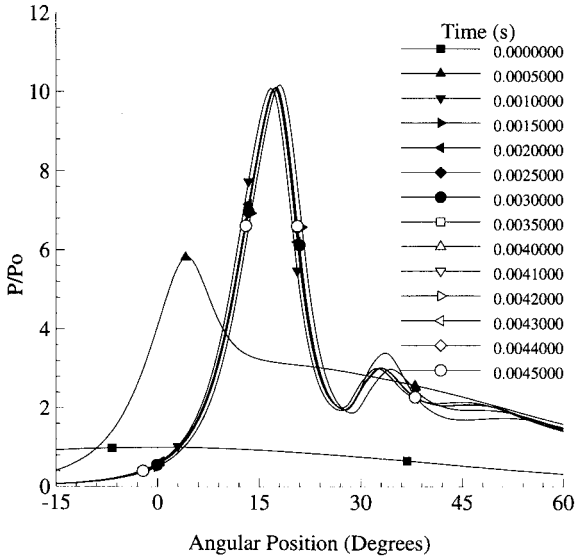

Fig. 16 Time history ($t \leq 4.5$ ms) of the surface pressure for θ_s = 174.0 deg.

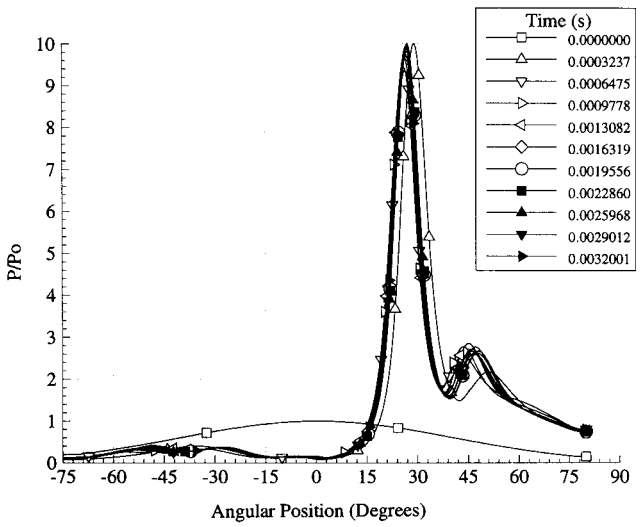

Fig. 17 Time history of the surface pressure for θ_s = 185.9 deg and $t < 3.2$ ms.

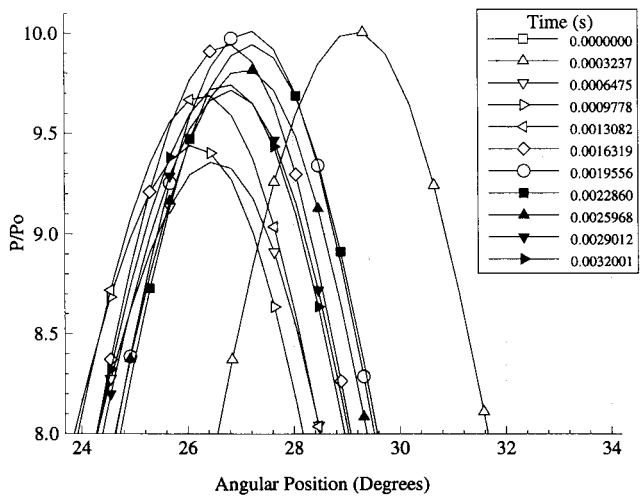

Fig. 18 Close view of time history of the surface pressure for θ_s = 185.9 deg showing the unsteady peak pressure region.

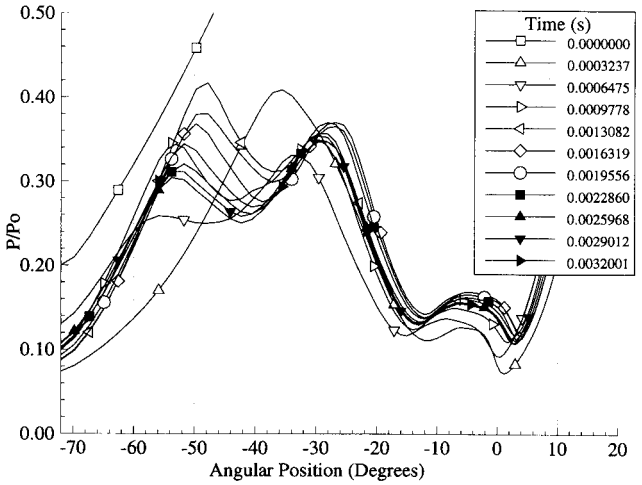

Fig. 19 Close view of time history of the surface pressure for θ_s = 185.9 deg showing the unsteady separation region.

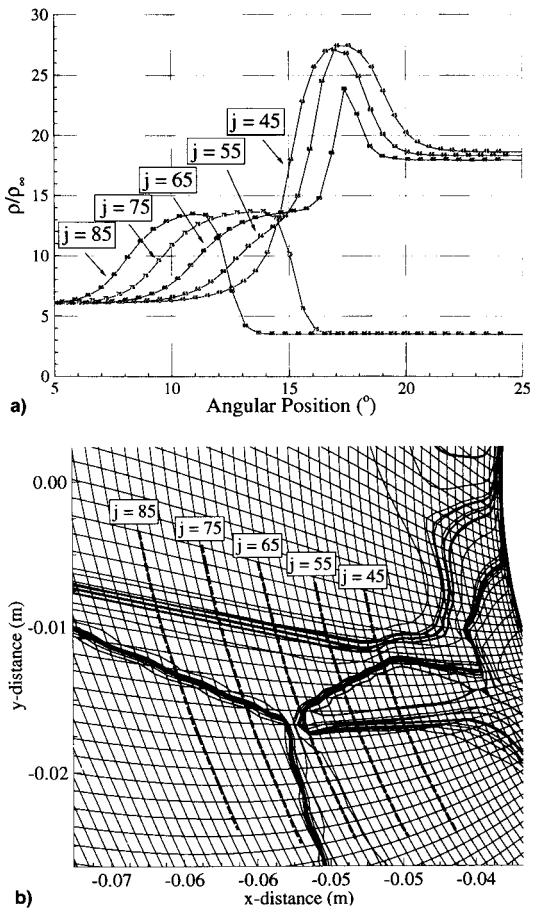

Fig. 20 Variation of a) density along select paths as described in the plot of b) Mach number contours for θ_s = 170.0 deg.

and position of the peak surface pressure, while others continued to oscillate. Figure 10b compares the peak pressure distribution for one of the unsteady cases, θ_s = 175.7 deg, with the steady cases and highlights the oscillatory behavior. The cases for $\theta_s > 180$ deg are shown in Fig. 11. A comparison of the jet impingement angle (JIA) and the peak surface pressure for the cases studied in this work determined to be unsteady are shown in Fig. 12.

In general, Figs. 10–12b show that the peak surface pressure and the position of the peak surface pressure are slightly out of phase and that the interaction with the greatest am-

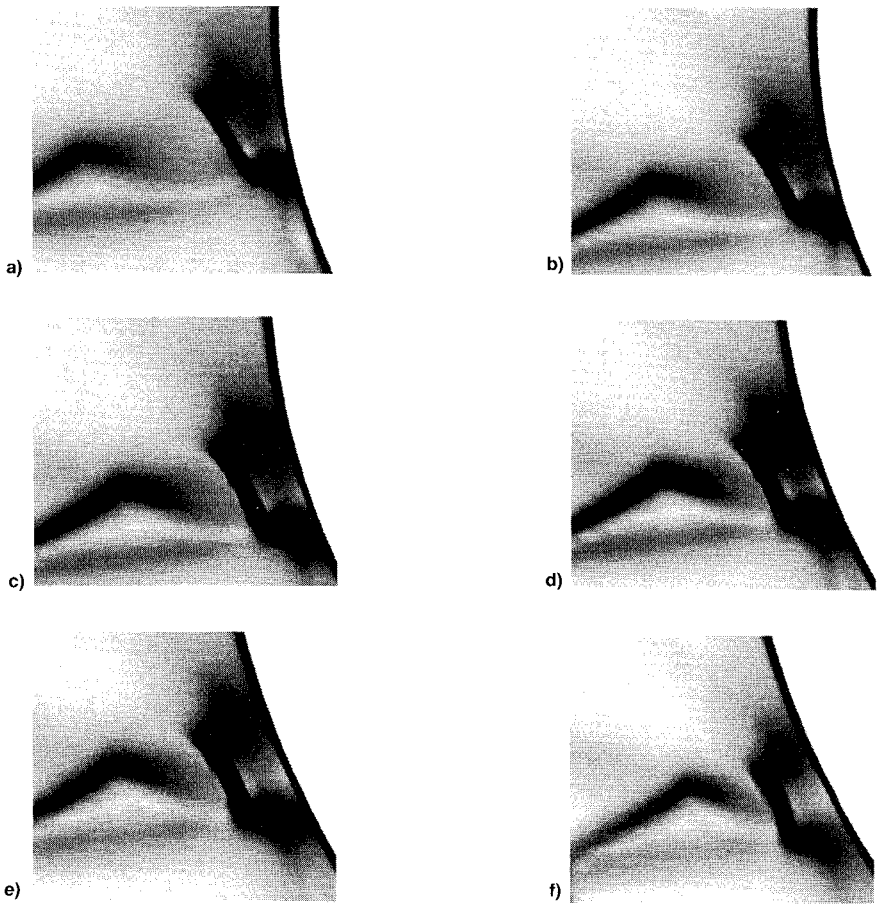

Fig. 21 Computational schlieren of the terminating shock associated with the supersonic jet for various shock impingement locations: θ_s = a) 168.2, b) 171.2, c) 175.7, d) 179.1, e) 182.9, and f) 185.9 deg.

plitude in the peak pressure is associated with the case with the greatest shock impingement location θ_s. For the cases in which $\theta_s \geq 171.2$ deg, increasing the impinging shock location tended to increase the peak transient surface pressure, decrease the steady-state surface pressure, increase the rate of convergence to the peak pressure associated with the transient phase, and increase the angular position of the impinging jet.

Figures 10–12b also show that there is a low-frequency transient as well as a high-frequency "steady-state" motion associated with the interaction. This is shown schematically in Fig. 13. The effect of θ_s on the frequency of oscillation is summarized in Fig. 14. This figure shows that there is a direct relationship between the oscillation frequency and the location of the impinging shock.

A time history of the surface pressure, for $\theta_s = 174.0$ deg, is shown in Fig. 15 for $t \leq 1$ ms in steps of 0.1 ms. Figure 16 is a similar plot, but for $t \leq 4.4$ ms in steps of 0.5 ms. It is important to note the rate at which the solution reaches the steady state, which should be compared with the previous figures.

Figures 17–19 describe the time history of the surface pressure for the unsteady case in which $\theta_s = 185.9$ deg for $t <$ 3.2 ms. Notice that after 1 ms the solution converges to a quasisteady state, oscillating about a mean angular position of about 27 deg. For this case the unsteadiness appears to be caused by an unstable separation region located around $\theta = -40$ deg, as shown in Fig. 19. The oscillation frequency was determined to be about 2.4 kHz, which corresponds to the low-frequency oscillation described in Fig. 14.

Detailed Flowfield Analysis

In order to better understand the type IV shock interaction phenomena, particularly the region where the supersonic jet impinges, detailed flowfield calculations were performed. Resolution of the key interaction features (shocks and shear layers) is shown in Fig. 20 for the case in which $\theta_s = 170.0$ deg. Figure 20a describes the density variation along the selected grid lines that are highlighted in the Mach contour plot shown in Fig. 20b. These figures show that the shocks are captured within 5 grid points and the shear layers are captured in less than 10 grid points. This further shows the importance of grid clustering.

Recall that for certain shock impingement locations the interaction was determined to be unsteady. Close examination of the jet impingement region reveals interesting flowfield characteristics and suggests a possible explanation why some of the interactions were steady and others were unsteady. Computational schlierens of some of the interactions studied in this work are shown in Fig. 21. Comparison of Fig. 21 with Figs. 10–12b shows that for the configurations in which the jet was oscillating the terminating shock associated with the supersonic jet was angled slightly upward or downward. For the case where $\theta_s \approx 180$ deg the interaction was steady.

This has subsequently led to the following subdivision of the nomenclature used to describe the type IV shock interaction:

Type IV$^-$: for $\theta_s > 185$ deg
Type IV: for $175 < \theta_s < 185$ deg
Type IV$^+$: for $\theta_s < 175$ deg

Using this nomenclature, the type IV$^+$ was found to be steady, the type IV$^-$ unsteady, and the type IV may be steady or unsteady.

Conclusions

The unsteady characteristics of the type IV shock interaction have been numerically investigated using a time-accurate thin layer formulation of the Navier–Stokes equations coupled with a high-resolution, implicit TVD scheme.

Grid clustering is important to capturing the essential physics of the interaction. In addition to the surface gridding necessary to capture the boundary layer, it is also important to have sufficient gridding in the shock and shear layer regions.

The location of the impinging shock has a strong influence on the development of the interaction, on the maximum value of the peak pressure, and on the frequency of oscillation associated with the interaction. The unsteadiness associated with the type IV$^-$ interaction resulted from an unstable separation region located above the jet impingement location and to the orientation of the terminating shock associated with the supersonic jet. The unsteadiness associated with the type IV interaction, an inherent unsteadiness, appeared to only be related to the orientation of the terminating shock of the supersonic jet. It was also observed that when the terminating shock is oriented such that it is either parallel with the body surface or makes an angle such that the flow through the shock is deflected downward, the interaction was found to be unsteady.

Acknowledgments

A portion of this work was conducted under the support of NASA Langley Research Center, with Ajay Kumar as technical monitor, NASA Grant NAG-11333-S1. The authors would like to thank Helen Yee at the NASA Ames Research Center work for the use of the original TIMETVD code, John D. Anderson Jr. for many helpful discussions, and Arinder Judge for reviewing the original manuscript. Appreciation is also expressed to the JPL Supercomputing Center for their generous computing time and to the ONR Postdoctoral Fellowship Program.

References

[1]Bowcutt, K. G., "Optimization of Hypersonic Waveriders Derived from Cone Flows—Including Viscous Effects," Ph.D. Dissertation, Univ. of Maryland, College Park, MD, 1986.

[2]Edney, B., "Anomalous Heat Transfer and Pressure Distributions on Blunt Bodies at Hypersonic Speeds in the Presence of an Impinging Shock," Aeronautical Research Inst. of Sweden, FAA Rept. 115, 1968.

[3]Holden, M. S., Wieting, A. R., Moselle, J. R., and Glass, C., "Studies of Aerothermal Loads Generated in Regions of Shock/Shock Interaction in Hypersonic Flow," AIAA Paper 88-0477, Jan. 1988.

[4]Prabhu, R. K., Wieting, A. R., and Thareja, R. R., "Computational Studies of a Fluid Spike as a Leading Edge Protection Device for Shock-Shock Interference Heating," AIAA Paper 91-1734, June 1991.

[5]Prabhu, R. K., Stewart, J. R., and Thareja, R. R., "Shock Interference Studies on a Circular Cylinder at Mach 16," AIAA Paper 90-0606, Jan. 1990.

[6]Klopfer, G. H., and Yee, H. C., "Viscous Hypersonic Shock-on-Shock Interaction on Blunt Cowl Lips," AIAA Paper 88-0233, Jan. 1988.

[7]Gaitonde, D., and Shang, J. S., "The Performance of Flux-Split Algorithms in High-Speed Viscous Flows," AIAA Paper 92-0186, Jan. 1992.

[8]Lind, C. A., "A Computational Analysis of the Unsteady Phenomena Associated with a Hypersonic Type IV Shock Interaction," Ph.D. Dissertation, Dept. of Aerospace Engineering, Univ. of Maryland, College Park, MD, 1994.

[9]Keyes, J. W., and Hains, F. D., "Analytical and Experimental Studies of Shock Interference Heating in Hypersonic Flow," NASA TN D-7139, May 1973.

[10]Lind, C. A., and Lewis, M. J., "Sensitivity of Shock-Shock Interactions to Upstream Variations," *Journal of Propulsion and Power*, Vol. 7, No. 6, 1991, pp. 1074–1076.

[11]Nowak, R., Holden, M. S., and Wieting, A. R., "Shock/Shock Interference on a Transpiration Cooled Hemispherical Model," AIAA Paper 90-1643, June 1990.

[12]Lind, C. A., and Lewis, M. J., "A Numerical Study of the Unsteady Processes Associated with the Type IV Shock Interaction," AIAA Paper 93-2479, June 1993.

[13]Yee, H. C., and Harten, A., "Implicit TVD Schemes for Hyperbolic Conservation Laws in Curvilinear Coordinates," *AIAA Journal*, Vol. 25, No. 2, 1987, pp. 266–274.

[14]Yee, H. C., "A Class of High-Resolution Explicit and Implicit Shock-Capturing Methods," NASA TM 101088, Feb. 1989.

[15]Roe, P. L., "Approximate Riemann Solvers, Parameter Vectors, and Difference Schemes," *Journal of Computational Physics*, Vol. 43, March 1981, pp. 357–372.

[16]Pulliam, T. H., "Euler and Thin Layer Navier-Stokes Codes: ARC2D, ARC3D," *Notes for Computational Fluid Dynamics User's Workshop*, University of Tennessee Space Inst., E02-4005-023-84, March 1984.

[17]Montagne, J. L., and Yee, H. C., "Comparative Study of High-Resolution Shock-Capturing Schemes for a Real Gas," NASA TM 100004, July 1987.

[18]Billig, F. S., "Shock-Wave Shapes Around Spherical- and Cylindrical-Nosed Bodies," *Journal of Spacecraft and Rockets*, Vol. 4, June 1967, pp. 822, 823.

[19]Hoffmann, K. A., *Computational Fluid Dynamics for Engineers*, Engineering Education System, Austin, TX, 1989.

[20]Sorenson, R. L., "A Computer Program to Generate Two-Dimensional Grids About Airfoils and Other Shapes by the Use of Poisson's Equation," NASA TM 81198, May 1980.

[21]Hoffmann, K. A., Siddiqui, M. S., and Rutledge, W. H., "Effect of the Grid System on Heat Transfer Computations for High Speed Flows," *Numerical Grid Generation in Computational Fluid Dynamics and Related Fields*, Elsevier, New York, 1991.

[22]Holden, M. S., Moselle, J. R., and Lee, J., "Studies of Aerothermal Loads Generated in Regions of Shock/Shock Interaction in Hypersonic Flow," NASA CR-181893, Oct. 1991.